電気学会論文誌●（●●●●●●●部門誌）
IEEJ Transactions on ●●●●●●●●●●●●●●●●
Vol.●● No.● pp.●-●● DOI: ●.●●/ieejeiss.●●.●

Paper

V/f Control for Switched Reluctance Motor

Hirotaka Kato*a) Student Member, Takahiro Kumagai* Member
Jun-ichi Itoh* Senior Member, Keisuke Kusaka* Member
Masakazu Kato** Member

(Manuscript received Jan. 00, 20XX, revised May 00, 20XX)

This paper proposes a novel V/f control method for switched reluctance motor (SRM). The proposed method does not require rotor position information. In addition, the wide operating range including magnetic saturation region of the SRM and high torque/ampere ratio are achieved without complicated pre-measurement or finite element analysis (FEA). This paper proposed the following three methods and confirmed their effectiveness: (A) a virtual rotor magnetic flux is generated by controlling the zero-phase current with a PI controller, which realizes the V/f control for the SRM, (B) the damping control gain is designed to be stable at all operating points since the rotor magnetic flux and inductance value change dynamically according to the operating conditions, and (C) a high torque/ampere is achieved by applying both $i_0 = i_q$ control and $i_d = 0$ control. In the experiment, the proposed method achieved the stable operation in all N-T regions for the tested SRM. In addition, the current RMS value is reduced by 39% at the torque of 0.05p.u. compared with no MTPA control, which is the almost performance as the drive with the position sensor.

Keywords : Switched reluctance motor (SRM), MTPA control, V/f control, Stabilization method, Magnetic saturation

1. Introduction

A switched reluctance motor (SRM) is composed of only an iron core and windings without a permanent magnet using a rare earth, which is inexpensive to manufacture. The SRM has attracted attention as a variable-speed motor for industrial applications due to the robust salient pole structure of its rotor [1][2]. The variable-speed drive without a position sensor is expected for the SRM to take advantage of the high-temperature and high-speed durability and cost-effectiveness.

Many studies for the drive method without the rotor position sensor have been examined, which uses the position dependence on the inductance or flux linkage [3-8]. In this method, first, the instantaneous value of the inductance is detected from the voltage and the current. Next, the detected inductance is converted to the rotor position information based on the look-up table or the approximation formula of the relationship between the inductance and the rotor position. However, complicated control, such as the harmonic voltage superposition [3][4] or the additional analog circuit [5][6], is required to accurately detect the instantaneous value of the inductance. In addition, complicated pre-measurement or finite element analysis (FEA) is necessary to obtain the nonlinear magnetic model of the SRM [7][8] considering magnetic saturation. Recently, the driving method without a rotor position sensor including magnetic saturation region is practically essential for the miniaturization of a motor. Furthermore, the adjustment of the control parameters, such as the current amplitude, turn-on angle, and turn-off angle, is required for the design of the current and speed controllers with a high torque/ampere ratio, which requires pre-experiment or FEA [9][10].

This paper proposes a V/f control method for the SRM drive without the position sensor in order to solve the above problems. The V/f control essentially does not require the rotor position information due to its control strategy based on the rotating coordinate system relative to the converter output voltage. Therefore, the V/f control does not have the problem of the inductance detection accuracy and the conversion accuracy to the rotor position. Besides, the maximum torque/ampere (MTPA) control based on the maximum torque/ampere ratio in the field-oriented control for the SRM [11] is applied into the V/f control that achieves both simple speed control and high-efficiency drive without the rotor position sensor.

Although the principle of the proposed V/f control method for the SRM drive is based on the V/f control with the damping control and MTPA control proposed for the PMSM [12], the following features are mainly different. (A) It is necessary to generate a virtual rotor magnetic flux corresponding to the rotor magnet magnetic flux in the PMSM. (B) It is revealed for the damping control gain design method, which stabilizes the SRM in the whole operating area because the rotor magnetic flux and inductance change according to the operating conditions. Note that the effect of the magnetic saturation is simply considered by the magnetic characteristic at the aligned position which is obtained by simple pre-measurement without a locked rotor test, i.e., unnecessary of complicated pre-measurement and FEA. (C) It is necessary to apply not only i_d=0 but also i_0=i_q for the MTPA control.

In this paper, first, the proposed method for the above features of (A), (B), and (C) is explained. Next, the usefulness of the proposed

a) Correspondence to: Hirotaka Kato. E-mail: s203139+kato@nagaokaut.ac.jp
* Nagaoka University of Technology. 1603-1, Kamitomioka-machi, Nagaoka-shi, Niigata 940-2188, Japan
** Nagaoka Motor Development Co., Ltd. 16-2085, Nagaoka Business Incubation Center, Kukasawa-machi, Nagaoka-shi, Niigata 940-2135, Japan

V/f control method for the SRM drive is confirmed by the experimental results. In this paper, the parameters are designed under the assumption of a steady-state, because the SRM is expected to apply into fans, pumps and so on, which does not require a high torque response but only a speed control.

2. V/f control for Switched Reluctance Motor

Fig.1 shows the control diagram of the proposed V/f control for the SRM. The proposed method consists of (A) zero-phase current control, (B) V/f control, and (C) MTPA control. The details of each control are explained and designed in the following subsections.

2.1 Zero-phase Current Control

This paper develops a theory based on the mathematical model in the Field-Oriented Control (FOC, i.e. vector control) for the SRM, which is interpreted about, a virtual rotor magnetic flux is generated by DC component of an excitation current, and rotating magnetic field of the stator is generated by AC component of the excitation current.

In the zero-phase current control, the virtual rotor flux is generated by controlling the zero-phase current with a PI controller, which realizes the V/f control for the SRM described in Section 2.2.

2.2 V/f Control

Fig.2 shows the relationship between dq-axis and γδ-axis. The FOC of the SRM uses the dq-axis Cartesian coordinate system with the d-axis defined as the direction of the virtual rotor flux vector and the q-axis defined as the direction 90 degrees behind the d-axis. However, the V/f control uses the γδ-axis Cartesian coordinate system with the δ-axis defined as the direction of the converter output voltage and the γ-axis defined as the direction 90 degrees behind the δ-axis. Note that the defined γδ-axis in this paper is different from one in a sensor-less FOC. In the V/f control for the PMSM, the torque oscillation occurs due to the resonance between the moment of inertia and the armature inductance. Then, the torque oscillation is suppressed by the damping control, which feeds back the active current i_δ to the electric angular frequency command ω^*. In the SRM, the same damping control as that for the PMSM is achieved by generating the virtual rotor flux by the zero-phase current control.

This subsection first presents the simplified state equation of the SRM. Then, the inductance considering nonlinearity is obtained from simple approximation method. Finally, the cut-off frequency of the HPF and the damping gain are designed from the simplified state equation and the inductance.

The voltage equation and the torque equation in the γδ-axis Cartesian coordinate system are expressed as in (1) and (2), which are transformed from the equations in the dq-axis Cartesian coordinate system.

$$\boldsymbol{v} = R\boldsymbol{i} + \boldsymbol{L}_1 p\boldsymbol{i} + 2\omega \boldsymbol{L}_2 \boldsymbol{i} + 2p(\delta)\boldsymbol{L}_3 \boldsymbol{i} \quad \cdots\cdots (1)$$

where

$$\boldsymbol{v} = \begin{bmatrix} v_\gamma & v_\delta & v_0 \end{bmatrix}^T$$

$$\boldsymbol{i} = \begin{bmatrix} i_\gamma & i_\delta & i_0 \end{bmatrix}^T$$

$$\boldsymbol{L}_1 = \begin{bmatrix} L_\gamma & L_{\gamma\delta} & L_{\gamma 0} \\ L_{\delta\gamma} & L_\delta & L_{\delta 0} \\ L_{0\gamma} & L_{0\delta} & L_0 \end{bmatrix}$$

$$\boldsymbol{L}_2 = \begin{bmatrix} 2L_{\gamma\delta} & L_\delta - L_\gamma - L_{dc} & -L_{\delta 0} \\ L_\delta - L_\gamma + L_{dc} & -2L_{\gamma\delta} & L_{\gamma 0} \\ 0 & 0 & 0 \end{bmatrix}$$

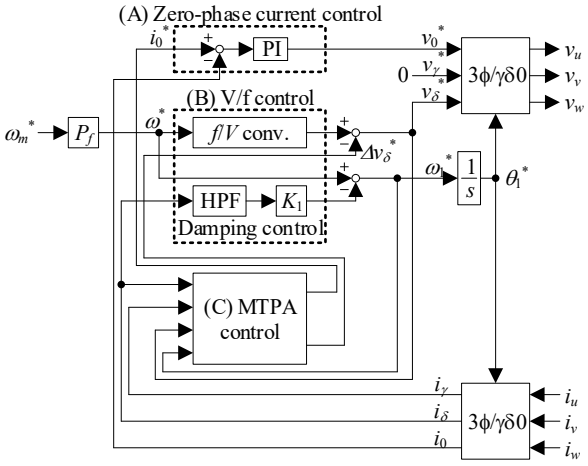

Fig. 1. V/f control method based on γδ axis.

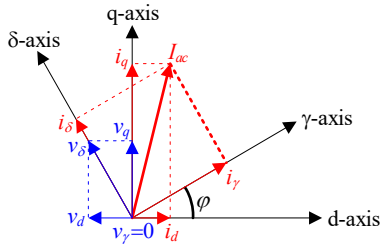

Fig. 2. Relationship between dq-axis and γδ-axis.

$$\boldsymbol{L}_3 = \begin{bmatrix} -L_{\gamma\delta} & L_\delta - L_{dc} & L_{\delta 0} \\ L_\delta - L_{dc} & L_{\gamma\delta} & -L_{\gamma 0} \\ L_{\delta 0} & -L_{\gamma 0} & 0 \end{bmatrix}$$

$$L_\gamma = L_{dc} + \frac{L_{dc}}{2}\cos(6\theta_1 - 2\varphi)$$

$$L_\delta = L_{dc} - \frac{L_{dc}}{2}\cos(6\theta_1 - 2\varphi)$$

$$L_0 = L_{dc}$$

$$L_{\gamma\delta} = L_{\delta\gamma} = -\frac{L_{dc}}{2}\sin(6\theta_1 - 2\varphi)$$

$$L_{\gamma 0} = L_{0\gamma} = \frac{L_{dc}}{\sqrt{2}}\cos(2\varphi)$$

$$L_{\delta 0} = L_{0\delta} = -\frac{L_{dc}}{\sqrt{2}}\sin(2\varphi)$$

$$T = \sqrt{2}PL_{ac}i_0 i_q = \sqrt{2}PL_{ac}i_0(i_\gamma \sin(2\varphi) + i_\delta \cos(2\varphi)) \quad \cdots\cdots (2)$$

R is the winding resistance, L_{dc} and L_{ac} are the dc and ac components of the self-inductance, respectively, p is the differential operator, φ is the deviation angle between the γδ-axis Cartesian coordinate and the dq-axis Cartesian coordinate, P is the number of pole pairs, and J is the moment of inertia. Note that the absolute transformation is applied.

The state equation is derived by first ignoring the asynchronous term appearing as sixth harmonic for simplification and then performing a linear approximation near the steady-state in the same way as Ref. [12], and expressed as in (3),

$$p\begin{bmatrix} \Delta i_\gamma \\ \Delta i_\delta \\ \Delta i_0 \\ \Delta\omega \\ \Delta\varphi \\ \Delta\chi \end{bmatrix} = \begin{bmatrix} A_{11} & A_{12} & A_{13} & A_{14} & A_{15} & A_{16} \\ A_{21} & A_{22} & A_{23} & A_{24} & A_{25} & A_{26} \\ A_{31} & A_{32} & A_{33} & A_{34} & A_{35} & A_{36} \\ A_{41} & A_{42} & A_{43} & A_{44} & A_{45} & A_{46} \\ A_{51} & A_{52} & A_{53} & A_{54} & A_{55} & A_{56} \\ A_{61} & A_{62} & A_{63} & A_{64} & A_{65} & A_{66} \end{bmatrix}\begin{bmatrix} \Delta i_\gamma \\ \Delta i_\delta \\ \Delta i_0 \\ \Delta\omega \\ \Delta\varphi \\ \Delta\chi \end{bmatrix} + \begin{bmatrix} B_{11} & B_{12} & B_{13} & B_{14} \\ B_{21} & B_{22} & B_{23} & B_{24} \\ B_{31} & B_{32} & B_{33} & B_{34} \\ B_{41} & B_{42} & B_{43} & B_{44} \\ B_{51} & B_{52} & B_{53} & B_{54} \\ B_{61} & B_{62} & B_{63} & B_{64} \end{bmatrix}\begin{bmatrix} \Delta v_\gamma \\ \Delta v_\delta \\ \Delta v_0 \\ \Delta\omega^* \end{bmatrix} \quad \cdots\cdots (3)$$

Note that the specific formulas for each element are shown in the appendix.

The deviation angle φ_0 at each operating point is expressed as in (4), assuming the MTPA control (i_d=0, i_0=i_q) is achieved which will be detailed below (The derivation is shown in the appendix).

$$\varphi_0 = \frac{1}{2}\arctan\left(\frac{\omega_0 L_{dc}}{0.5R + \omega_0 L_{ac}}\right) \quad \text{..... (4)}$$

where subscript "0" of the deviation angle φ and the electric angular frequency ω, represent that they are the steady-state value. Hereinafter subscript "0" shows the steady-state value. The γδ-axis current i_γ, i_δ at each operating point is expressed as in (5), using the zero-phase current i_{00} at its operating point and the deviation angle expressed at (4) (The derivation is shown in the appendix).

$$\begin{bmatrix} i_{\gamma 0} \\ i_{\delta 0} \end{bmatrix} = \begin{bmatrix} \frac{i_{00}}{\sqrt{2}}\sin(2\varphi_0) \\ \frac{i_{00}}{\sqrt{2}}\cos(2\varphi_0) \end{bmatrix} \quad \text{..... (5)}$$

The state equation of the SRM is determined by the electric angular frequency ω, the zero-phase current i_0, the motor parameters P, R, L_{dc}, L_{ac}, and cut-off frequency of the HPF ω_c at each operating point.

Table 1 shows the motor parameters. Fig.3 shows the frequency characteristics of the command speed to the motor speed under the base speed, which are obtained from (3) and the simulation. The test motor is an 18S/12P type SRM of 2.2 kW, 4800 rpm (=1p.u.), and 4.38 Nm (=1p.u.). In the simulation, the mathematical model presented in Reds. [11] is applied. Fig.3 assumes i_d=0 and i_0=i_q thanks to the MTPA control and the figure shows the three condition of the zero-phase current of 0.33p.u., 0.66p.u., and 1p.u. Besides, in the simulation results in Fig. 3, the characteristics are obtained by giving the motor the rated mechanical angular frequency ω_{m0} as the input to the mechanical angular frequency command ω_m^* and observing the response of the output speed ω_m. On the other hand, the analysis using (3) is conducted with the steady-state value of the state variable ω, denoted as the rated electrical angular frequency ω_0 ($P\omega_{m0}^*$=ω_0). Note that ω_{m0} and ω_m^* are not state variables. Note that, in Fig. 3, the characteristics were obtained with the damping control disabled in order to verify the frequency characteristics including the resonance. As shown in Fig.3, the calculation results by (3) and the simulation results are almost the same, i.e., the derived sixth-order equation of the state-model is valid.

In order to simplify the equation, the following conditions are assumed to discuss the stability and response.

(i) No-load condition: $\varphi = 0$, $i_\gamma = 0$, $i_\delta = 0$

(ii) High-speed rotation condition

: $\omega_0 L_{dc}$, $\omega_0 L_{ac} >> R$, $\omega_0 L_{dc} >> K_1 i_\delta$

(iii) The mechanical time constant is sufficiently larger than the electrical time constant: $p(\Delta i_\gamma) = 0$, $p(\Delta i_\delta) = 0$, $p(\Delta i_0) = 0$

(iv) The effect of the HPF on the stability is small: $p(\Delta x) = 0$

The natural angular frequency ω_n and the damping factor ζ are calculated from the characteristic equation of the second-order system, which is derived by approximating the derived sixth-order state equation expressed as in (1) as a second-order system from the assumption of from (i) to (iv), and expressed as in (6),

$$[\omega_n, \varsigma] = \left[\frac{2P\Phi_r}{\sqrt{JL_{dc}}}, \frac{2}{P}\sqrt{\frac{J}{L_{dc}}}K_1\right] \quad \text{..... (6)}$$

Table 1. Motor parameters of test motor.

Rated power	2.2kW
Base speed(1p.u.), Max. speed	4800rpm, 7200rpm
Max. torque(1p.u.)	4.38Nm
DC voltage	300V
Poles	Stator:18, Rotor:12
Inertia	62.3×10^{-4}kgm^2
Resistance	0.66Ω
DC inductance	7.82mH
AC inductance	5.19mH
Rated current(1p.u.)	7.7A(i_{0Max}, i_{qMax})

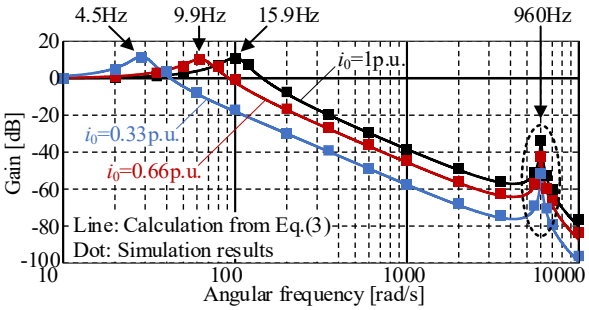

Fig. 3. Frequency characteristics of speed command to motor speed at base speed (1p.u.) with i_0=i_q, i_d=0.

where

$$\Phi_r = \frac{L_{ac}}{\sqrt{2}} i_0 \quad \text{..... (7)}$$

where K_1 is the damping gain, Φ_r is the virtual rotor flux, and i_0 is the zero-phase current. As shown in (6), the damping factor ζ is the function of the feedback gain K_1. In other words, the proposed V/f control is stabilized by setting K_1 appropriately. Comparing the natural angular frequency and the damping factor in the IPMSM [12], the rotor magnet magnetic flux corresponds to the virtual rotor magnetic flux in case of considering the difference of the coefficient by the transformation methods which are the absolute transformation and the reactive transformation. In addition, the q-axis inductance corresponds to the dc components of the self-inductance L_{dc}.

In this paper, the cut-off frequency of the HPF for the damping control is set to 1/20 of the natural frequency ω_n [13][14]. The sufficiently small HPF cutoff frequency prevents steady speed deviation while suppressing oscillation of the effective current (torque) due to the resonance. The HPF rejects the DC component and extracts the resonance component. Note that in case of the SRM, ω_n is changed by the zero-phase current as shown in (6). Therefore, the cut-off frequency of the HPF is designed from the lower-limit value of i_0 (i_{0Low}) in order to be always lower enough compared with the ω_n, even when i_0 is changed. In this paper, i_{0Low} is defined to 1/10 of i_{0Max} in order that phase-current is always bigger than zero even under the light loading condition. The cut-off frequency of the HPF ω_c is expressed as in (8).

$$\omega_c = \frac{\omega_n}{20} = \frac{1}{20}\frac{2P}{\sqrt{JL_{dc}}}\frac{L_{ac}}{\sqrt{2}} i_{0Low} = \frac{1}{20}\frac{2P}{\sqrt{JL_{dc}}}\frac{L_{ac}}{\sqrt{2}}\frac{i_{0Max}}{10} \quad \text{..... (8)}$$

The cut-off frequency of the HPF is determined by motor parameters P, L_{dc}, L_{ac}, and rated zero-phase current i_0.

The self-inductance L_{dc} and L_{ac} are necessary to obtain the controller parameters. This paper adopts simple approximation method for the inductance to consider the magnetic saturation. The magnetic characteristic at the aligned position, at which the magnetic characteristic has the strongest nonlinearity, is acquired

from the measured current when one pulse voltage is injected. The magnetic characteristic at the aligned position is expressed as in (9), using a polynomial approximation.

$$\Phi_a = \sum_{n=1}^{N} k_n i^n \quad \cdots\cdots (9)$$

where k_n is each coefficient of the polynomial approximation and N is a maximum order of the polynomial approximation. N have to be relatively high order in order that the magnetic characteristic at the aligned position is expressed accurately. N is determined by the approximation accuracy of the magnetization curve and is 10 in this pater. Since the maximum current value I_{max} is expressed as twice the zero-phase current i_{00} (I_{max}=2*i_{00}), assuming the MTPA control (i_d=0, i_0=i_q) is achieved as detailed in detail below, the average inductance at the aligned position is expressed as in (10),

$$L_a(i_{00}) = \frac{\Phi_a(I_{Max})}{I_{Max}} = \sum_{n=1}^{N} k_n I_{Max}^{\,n-1} = \sum_{n=1}^{N} k_n (2i_{00})^{n-1} \quad \cdots\cdots (10)$$

DC and AC components of self-inductance considering the magnetic saturation L_{dc}, L_{ac} are expressed from the inductance at the aligned and unaligned position L_a, L_u as in (11),

$$[L_{ac}(i_{00}), L_{dc}(i_{00})] = \left[\frac{L_a(i_{00}) - L_u}{2}, \frac{L_a(i_{00}) + L_u}{2}\right] \quad \cdots\cdots (11)$$

The analysis is performed by substituting (11) into (1) to (8), which allows us to take magnetic saturation into account.

Fig.4 shows the loot locus of the sixth-order state equation when the damping gain K_1 is increased at the rated-load and the base speed. Note that from No. 1 to No.6 are the characteristic roots of the sixth-order state equation. As shown in Fig.4, poles named No.1 and 2 move toward the right-half plane as K_1 decreases. On the other hand, No.3 and 4 move toward the right-half plane as K_1 increases.

From Fig.4, following three variables are define:

(i) Lower-limit value of K_1, K_{1Low}
: The SRM is at the stability limit caused by No.1 and 2, when K_1=K_{1Low}.

(ii) Most stable value of K_1, $K_{1Stb.}$
: The dominant poles of the SRM have the farthest from the imaginary axis when K_1= $K_{1Stb.}$. In this condition, the real part of the poles No. 1, 2, 3, and 4 matches.

(iii) Upper-limit value of K_1, K_{1Up}
: The SRM is at the stability limit caused by No.3 and 4 when K_1=K_{1Up}.

Note that suppression of the overshoot of the motor rotation speed is achieved by the same way as Refs. [13][14].

Fig.5 shows the relationship with the zero-phase current and the K_{1Low}, $K_{1Stb.}$, and K_{1Up}. In case of the SRM, $K_{1Stb.}$ is changed by the zero-phase current. Although the transient response is improved in case that K_1 is adjusted to $K_{Stb.}$ according the zero-phase current, control system would be complex. Therefore, K_1 is set to be within the stable value in all conditions and the closest value with $K_{Stb.}$.

Fig.6 shows the flowchart of the design of the damping gain K_1. The moment of inertia J, the number of pole pairs P, and rated zero-phase current i_0 is input constants. First, the inductance at the unaligned position and the resistance, which is independent of the current is measured. Second, the i-Φ_a(ι) characteristic at the aligned position is derived with the approximation, as shown in (9). This characteristic is acquired by the injection of the one pulse voltage.

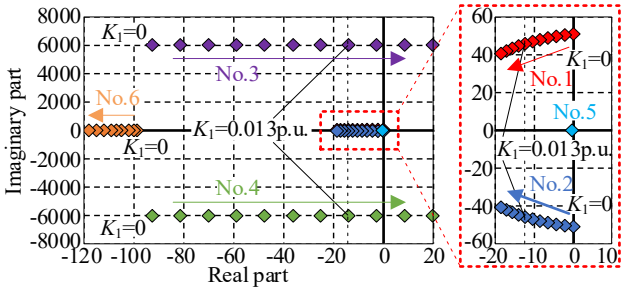

Fig. 4. Loot locus of sixth-order state equation when damping gain K_1 is increased at base speed (1.0p.u.) with i_0=i_q, i_d=0.

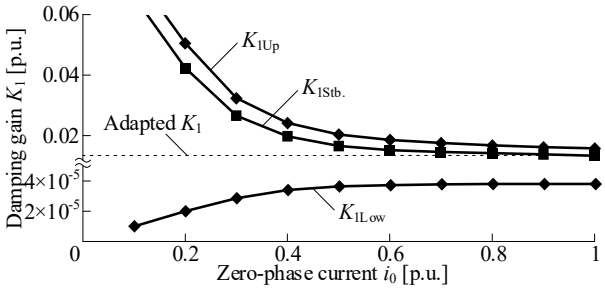

Fig. 5. Relationship between zero-phase current and damping gain K_1.

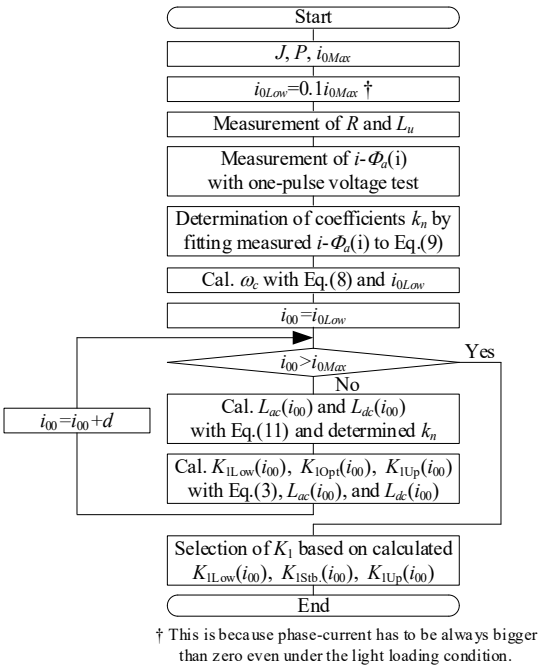

† This is because phase-current has to be always bigger than zero even under the light loading condition.

Fig. 6. Design flow of damping gain K_1.

This measurement relatively easy compared to the complicated pre-measurement including the locked rotor test or the FEA. Third, the cut-off frequency of the HPF is calculated from the lower-limit value of the zero-phase current i_{0LOW} and (8). Then, lower-limit value K_{1Low}, most stable value $K_{1Stb.}$, and upper-limit value K_{1Up} of the damping gain are calculated in the different zero-phase current from the lower-limit value i_{0LOW} to the rated value i_{0Max}. Finally, K_1 to stabilize the SRM is adopted.

2.3 Maximum Torque/Ampere (MTPA) Control

Fig.7 shows the control diagram of the MTPA control for the SRM. The MTPA control improves the torque/ampere ratio by adjusting the converter output voltage. The following conditions achieve the maximum torque/ampere ratio in the SRM.

$$i_0 = \sqrt{2} i_q \quad \text{..... (12)}$$

$$i_d = 0 \quad \text{..... (13)}$$

Note that the zero-phase current is larger than AC current amplitude because this paper uses the asymmetric half-bridge converter for the unipolar driving and negative current does not flow ($\sqrt{2}$ in (12) is the coefficient of the park transformation.). Therefore, it is necessary to apply not only i_d=0 but also i_0=i_q for the MTPA control.

First, the i_0=i_q control is explained. i_q is equal to the AC current amplitude I_{ac} when i_0=0. Thus, i_0 should be controlled to I_{ac} not to flow the negative current. The command value of zero-phase current control is expressed as (14).

$$i_0^* = \sqrt{2} i_q = \sqrt{2} I_{ac} = \sqrt{2}\sqrt{i_\gamma^2 + i_\delta^2} \quad \text{..... (14)}$$

where i_γ and i_δ are the γ-axis and δ-axis current, respectively.

Next, the i_d=0 control is explained. The i_d=0 control is achieved indirectly in the γδ-axis coordinate by focusing on the reactive power of the SRM. In the dq-axis coordinate, the reactive power Q_{dq} input into the SRM is expressed as in (15).

$$Q_{dq} = v_q i_d - v_d i_q = 2\omega\left\{L_{dc}(i_d^2 + i_q^2) + L_{ac} i_0 i_d / \sqrt{2}\right\} \quad \text{..... (15)}$$

where v_d and v_q are the d-axis and q-axis voltage respectively. The reactive power Q_{dq} under the condition of i_d=0 is expressed as in (16),

$$Q_{dq} = 2\omega L_{dc} i_q^2 = 2\omega L_{dc} I_{ac}^2 = 2\omega L_{dc}(i_\gamma^2 + i_\delta^2) \quad \text{..... (16)}$$

On the other hand, in the γδ-axis coordinate, the reactive power $Q_{\gamma\delta}$ is expressed as in (17),

$$Q_{\gamma\delta} = v_\delta i_\gamma \quad \text{..... (17)}$$

Therefore, the v_δ should be adjusted by the P controller in order to match the reactive power $Q_{\gamma\delta}$ calculated by (17) to the reactive power Q_{dq} calculated by (16). As shown in Fig.7, the value calculated by (14) is applied as the command value for zero-phase current control for the i_0=i_q control. On the other hand, the deviation between (16) and (17) is regulated to be zero by adjusting the v_δ with the P controller for the i_d=0 control. Note that the LPF in the second stage of the P controller shown in Fig.7 is to achieve the i_d=0 control at a steady-state by reducing the gain for high frequencies [12]-[14]. In addition, the limit is provided in order to prevent overcompensation.

3. Experimental Results

Fig. 8 shows the experimental system. As shown in Fig.8(a), the load motor outputs the arbitrary constant torque. In addition, the instantaneous torque is measured by a high-response torque meter (UTMII-10 Nm, 1 kHz bandwidth, UNIPULSE). As shown in Fig.8(b), the controller consists of an interface board, 12bit Analog Digital converter (A/D), Digital Signal Processor (DSP), and Pulse Width Modulation (PWM) module. The greatest part of the proposed V/f control is implemented on the DSP. Exceptionally, only A/D conversion of the detected current and the generation of PWM signal based on voltage command are performed by dedicated parts. On the other words, the proposed method composed only of a general purpose micro-computer and does not require a high-speed

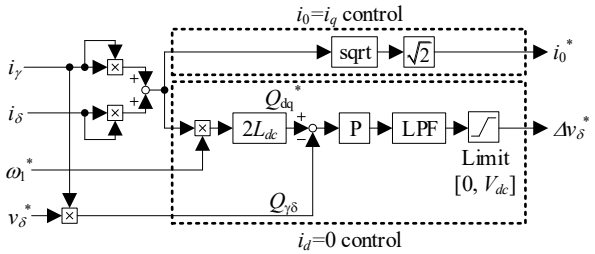

Fig. 7. Control diagram of MTPA control.

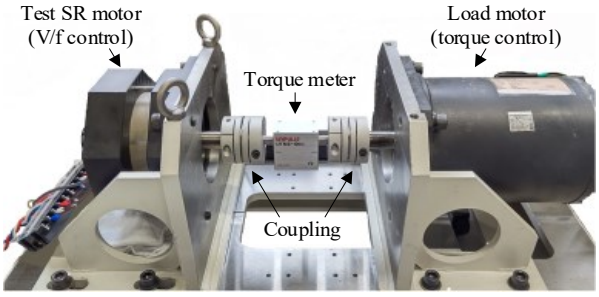

(a) Experimental system

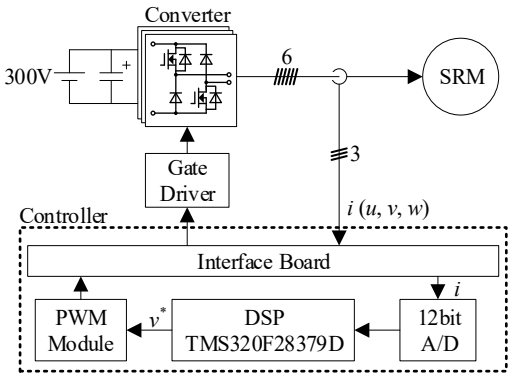

(b) Control system

Fig. 8. Configuration of test system.

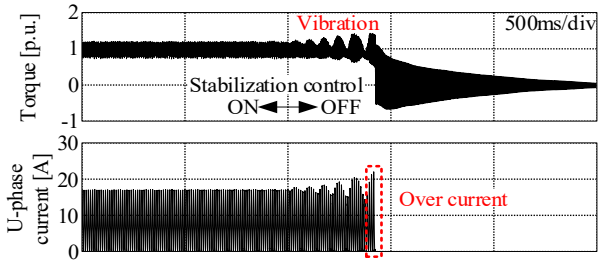

Fig. 9. Effect of damping control.

computing device such as Field Programmable Gate Array (FPGA). In "V/f conv" in Fig.1, the V/f ratio is set so that the provisional modulation index is 1 at the base speed (1p.u.). Note that its modulation index is adjusted in the MTPA control.

Fig. 9 shows the effect of the damping control. Speed and torque are 1p.u. In the section with the damping control, there is no oscillation in the U-phase current and torque. On the other hand, the oscillation occurs after disabling the damping control. These results indicate the effectiveness of the damping control.

Fig.10 shows the experiment results that startup is achieved with 1p.u. torque from zero-speed to base speed. The motor is accelerated by the boost voltage after the zero-phase current of the rated value i_{0Max} was generated by the PI control at the stop condition. Note that the fine vibration, which is different from the mechanical resonance frequency ωn, is superimposed on the torque waveform. This is due to the torsional resonance in the experimental system excited by the torque step in the startup. (The detail is explained in the appendix). As a result, the acceleration with the rated torque (i.e. rated acceleration time) is achieved. Although the step-out does not occur, the torque is oscillating because the torque changes rapidly at the start and finish of acceleration. This is because each control system is designed under the steady-state. The design of the control system considering including the transient response is a future issue.

Fig.11 shows the step response for 0.5p.u. torque at rated speed. The motor follows the load without stepping out. Note that the motor will step out with this control at step torques of 0.5p.u. or more because the control system is designed with a low bandwidth assuming the steady-state.

Fig.12 shows the speed and torque curves and Fig.13 shows the torque and U-phase current at the rated speed and Max. speed condition. The proposed method achieved to drive at 1p.u. torque and at from 0.1p.u. to 1p.u. speed. In addition, the proposed method drives with the rated power at from 1p.u. to 1.5p.u. speed. Note that the rated torque is not output at the 0.1p.u. speed or lower because of the output voltage error due to the dead time.

Fig.14 shows the effect of the MTPA control at the speed of 0.1p.u. The current of the proposed method (V/f control with $i_0=i_q$ and $i_d=0$) is compared with that of the FOC with $i_0=i_q$ and $i_d=0$ and that of V/f control with only $i_0=i_q$. The current RMS value is reduced by 39.0% compared with the only $i_0=i_q$ control at the torque of 0.05p.u. The proposed drive without the position sensor brings out the same performance as the drive with the position sensor. On the other hand, the current RMS value is increased by 14.6% compared with the FOC with the position sensor. There are three reasons why the current of the proposed method increases more than that of the FOC in the low-torque region. One reason is that the control accuracy deteriorates as the input power decreases and the reactive power decreases in the low torque conditions. The other reasons are the use of the proportional controller in Fig. 7 and setting the lower limit on the zero-phase current. In this paper, the comparison of the current RMS value with the torque is presented in order to validate the effect of the MTPA control. Since the iron loss accounts for a larger proportion of the total loss at the high speeds, minimizing the loss including the iron loss is necessary to maximize the efficiency. The exploration of the loss minimization control is a subject for future work.

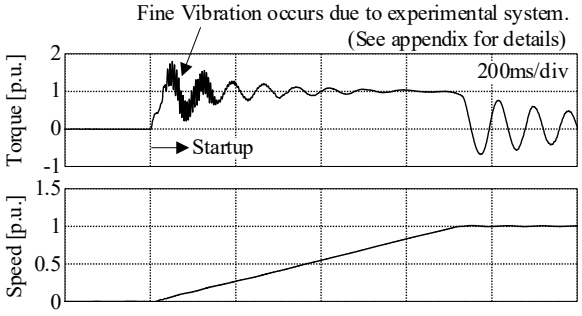

Fig. 10. Startup at i_0, i_q=1.0p.u.

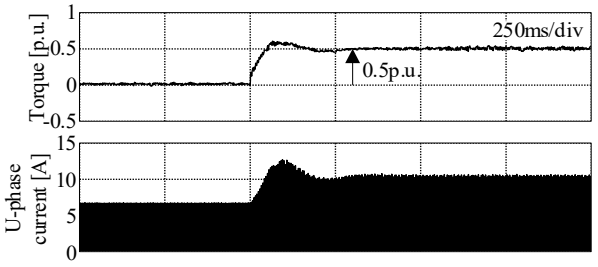

Fig. 11. Step response for 0.5p.u. torque.

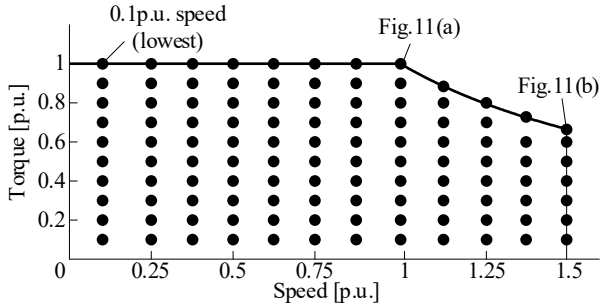

Fig. 12. Speed and torque curves.

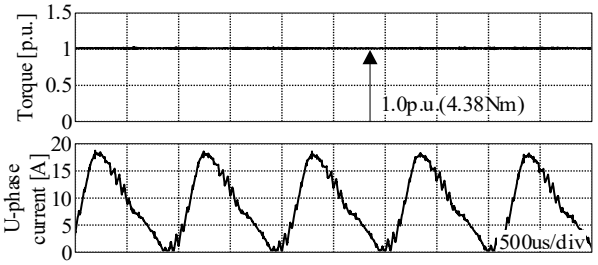

(a) 1p.u. torque, 1p.u. speed
(b)

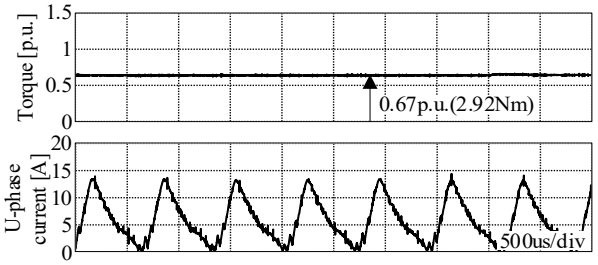

(b) 0.67p.u. torque, 1.5p.u. speed

Fig. 13. Torque and U-phase current waveform.

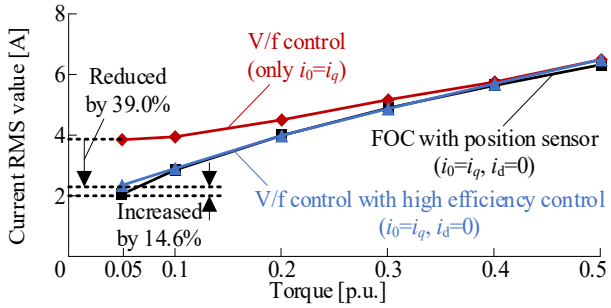

Fig. 14. Effect of MTPA control (0.1p.u. speed).

4. Conclusions

This paper proposed a novel V/f control method for the SRM. This paper proposed the following three methods and confirmed their effectiveness: (i) the virtual rotor magnetic flux is generated by controlling the zero-phase current with the PI controller, which realizes the V/f control for the SRM, (ii) the damping control gain is designed to be stable at all operating points even when the rotor magnetic flux and the inductance value changes dynamically according to the operating conditions, and (iii) the high torque/ampere is achieved by applying both the $i_0 = i_q$ control and $i_d = 0$ control. In the experiment, the proposed method achieved the stable operation in all N-T regions with the tested SRM. In addition, the current RMS value is reduced by 39% at the 0.05p.u. torque compared with the case of no MTPA control, which is the almost same performance as the driving with the position sensor.

References

(1) T. Kosaka, A. Kume, H. Wakayama, and N. Matsui: "Development of high torque density and efficiency vswitched reluctance motor with 0.1mm short airgap", 2007 European Conference on Power Electronics and Applications, pp. 1-9 (2007)

(2) H. Yamai, Y. Sawada, and K. Ohyama: "Applying Switched Reluctance Motor to Oil Hydraulic Pump Use", IEEJ Trans. on Ind. Applicat., Vol.123, No.2, pp.96-104 (2003)

(3) K.-W. Hu, Y.-Y. Chen, and C.-M. Liaw: "A reversible position sensorless controlled switched-reluctance motor drive with adaptive and intuitive commutation tunings", IEEE Trans. Power Electron., Vol.30, No.7, pp.3781-3793 (2015)

(4) K. Ha, R.Y. Kim, and R. Krishnan: "Position estimation in switched reluctancemotor drive using the first switching harmonics through fourier series", IEEE Trans. Ind. Electron., Vol.58, No.12, pp.5352–5360 (2011)

(5) G.G. Lopez, P.C. Kjaer, and T.J.E. Miller: "A new sensorless method for switched reluctancemotor drives", IEEE Trans. Ind. Applicat., Vol.34, No.4, pp.832–840 (1998)

(6) S. Sumita, K. Deguchi, and Y. Iwaji: "Position Sensorless Control Method for SRM Using Analog Circuit of Type-1 Control System", IEEJ Trans. Ind. Applicat., Vol.137, No. 8, pp.612-621 (2017)

(7) T. Kosaka, K. Ochiai, and N. Matsui: "Sensorless Control of SRM using Magnetizing Curves", IEEJ Trans. Ind. Applicat., Vol.120, No.2, pp.216-222 (2000)

(8) T. Kosaka, Y. Nabeya, K. Ohyama, and N. Matsui: "Position Sensorless Drive of SRM Mounted on Hydraulic Pump Unit", IEEJ Trans. Ind. Applicat., Vol.123, No.2, pp.103-111 (2003)

(9) K.M. Rahman, B. Fahimi, G. Suresh, A.V. Rajarathnam, and M. Ehsani: "Advantages of Switched Reluctance Motor Applications to EV and HEV: Design and Control Issues", IEEE Trans. on Ind. Applicat., Vol.36, No.1, pp.111–121 (2000)

(10) I. Husain and S.A. Hossain: "Modeling, Simulation, and Control of Switched Reluctance Motor Drives", IEEE Trans. on Ind. Electron., Vol.52, No.6, pp.1625–1634 (2005)

(11) N. Nakao and K. Akatsu: "Vector Control Specialized for Switched Reluctance Motor Drives", IEEE Trans. on Ind. Applicat., Vol.134, No.12, pp.1006–1015 (2014)

(12) J. Itoh, J. Toyosaki, and H. Ohsawa: "High performance V/f control method for PM Motor", Vol.122, No.3, pp.235-259 (2002)

(13) T. Toi, M. Kato, and J. Itoh: "Parameter Design Considering Loot Locus for Damping Control Based on V/f control of IPMSM", 2016 Kansai-section Joint Convention of Institutes of Electrical Engineering, No. G4-22 (2016)

(14) T. Toi, K. Nishizawa, and J. Itoh: "Stabilization Method for IPMSM with Long Electrical Time Constant Using Equivalent Resistance Gain Based on V/f Control", IEEJ Transactions on Industry Applications, Vol. 8, No. 4, pp. 592-599 (2019)

Appendix

1. State equation of the SRM

Each element of the state equation (3) are expressed as follows. Note that the subscript "0" indicates the value of the operating point in each variable.

$$A_{11} = \frac{-R\left(L_{dc}^{\ 2} - \frac{L_{ac}^{\ 2}}{2}\sin^2(2\varphi_0)\right) - 2\omega_0\left(-\frac{L_{dc}L_{ac}^{\ 2}}{2}\sin(2\varphi_0)\cos(2\varphi_0)\right)}{L_{dc}^{\ 3} - \frac{L_{dc}L_{ac}^{\ 2}}{2}} \quad \text{(A-1)}$$

$$A_{12} = \frac{-R\left(-\frac{L_{ac}^{\ 2}}{2}\sin(2\varphi_0)\cos(2\varphi_0)\right) - 2\omega_0\left(-L_{dc}^{\ 3} + \frac{L_{dc}L_{ac}^{\ 2}}{2}\sin^2(2\varphi_0)\right) - 2K_1(L_{dc}^{\ 3} - \frac{L_{dc}L_{ac}^{\ 2}}{2})i_{\delta 0}}{L_{dc}^{\ 3} - \frac{L_{dc}L_{ac}^{\ 2}}{2}} \quad \text{(A-2)}$$

$$A_{13} = \frac{-R\left(-\frac{L_{dc}L_{ac}}{\sqrt{2}}\cos(2\varphi_0)\right) - 2\omega_0\frac{1}{\sqrt{2}}\left(L_{dc}^{\ 2}L_{ac} - \frac{L_{ac}^{\ 3}}{2}\right)\sin(2\varphi_0)}{L_{dc}^{\ 3} - \frac{L_{dc}L_{ac}^{\ 2}}{2}} \quad \text{(A-3)}$$

$$A_{14} = \frac{-2\left\{\left(-\frac{L_{dc}L_{ac}^{\ 2}}{2}\sin(2\varphi_0)\cos(2\varphi_0)\right)i_{\gamma 0} + \left(-\frac{L_{dc}L_{ac}^{\ 2}}{2}\cos^2(2\varphi_0)\right)i_{\delta 0} + \frac{1}{\sqrt{2}}\left(L_{dc}^{\ 2}L_{ac} - \frac{L_{ac}^{\ 3}}{2}\right)\sin(2\varphi_0)i_{00}\right\}}{L_{dc}^{\ 3} - \frac{L_{dc}L_{ac}^{\ 2}}{2}}$$

$$\text{(A-4)}$$

$$A_{15} = \frac{-4\omega_0\left\{\frac{L_{dc}^{\ 2}L_{ac}}{\sqrt{2}}\cos(2\varphi_0)i_{00}\right\}}{L_{dc}^{\ 3} - \frac{L_{dc}L_{ac}^{\ 2}}{2}} \quad \text{(A-5)}$$

$$A_{16} = 2K_1 i_{\delta 0} \quad \text{(A-6)}$$

$$A_{21} = \frac{-R\left(-\frac{L_{ac}^{\ 2}}{2}\sin(2\varphi_0)\cos(2\varphi_0)\right) - 2\omega_0\left(L_{dc}^{\ 3} - \frac{L_{dc}L_{ac}^{\ 2}}{2}\cos^2(2\varphi_0)\right)}{L_{dc}^{\ 3} - \frac{L_{dc}L_{ac}^{\ 2}}{2}} \quad \text{(A-7)}$$

$$A_{22} = \frac{-R\left(L_{dc}^{\ 2} - \frac{L_{ac}^{\ 2}}{2}\cos^2(2\varphi_0)\right) - 2\omega_0\left(\frac{L_{dc}L_{ac}^{\ 2}}{2}\sin(2\varphi_0)\cos(2\varphi_0)\right) + 2K_1(L_{dc}^{\ 3} - \frac{L_{dc}L_{ac}^{\ 2}}{2})i_{\gamma 0}}{L_{dc}^{\ 3} - \frac{L_{dc}L_{ac}^{\ 2}}{2}} \quad \text{(A-8)}$$

$$A_{23} = \frac{-R\left(\frac{L_{dc}L_{ac}}{\sqrt{2}}\sin(2\varphi_0)\right) - 2\omega_0\frac{1}{\sqrt{2}}\left(L_{dc}^{\ 2}L_{ac} - \frac{L_{ac}^{\ 3}}{2}\right)\cos(2\varphi_0)}{L_{dc}^{\ 3} - \frac{L_{dc}L_{ac}^{\ 2}}{2}} \quad \text{(A-9)}$$

$$A_{24} = \frac{-2\left\{\left(\frac{L_{dc}L_{ac}^{\ 2}}{2}\sin^2(2\varphi_0)\right)i_{\gamma 0} + \left(\frac{L_{dc}L_{ac}^{\ 2}}{2}\sin(2\varphi_0)\cos(2\varphi_0)\right)i_{\delta 0} + \frac{1}{\sqrt{2}}\left(L_{dc}^{\ 2}L_{ac} - \frac{L_{ac}^{\ 3}}{2}\right)\cos(2\varphi_0)i_{00}\right\}}{L_{dc}^{\ 3} - \frac{L_{dc}L_{ac}^{\ 2}}{2}}$$

$$\text{(A-10)}$$

$$A_{25} = \frac{-4\omega_0\left\{-\frac{L_{dc}^{\ 2}L_{ac}}{\sqrt{2}}\sin(2\varphi_0)i_{00}\right\}}{L_{dc}^{\ 3} - \frac{L_{dc}L_{ac}^{\ 2}}{2}} \quad \text{(A-11)}$$

$$A_{26} = -2K_1 i_{\gamma 0} \quad \text{(A-12)}$$

$$A_{31} = \frac{-R\left(-\frac{L_{dc}L_{ac}}{\sqrt{2}}\cos(2\varphi_0)\right) - 2\omega_0\left(\frac{L_{dc}^{\ 2}L_{ac}}{\sqrt{2}}\sin(2\varphi_0)\right)}{L_{dc}^{\ 3} - \frac{L_{dc}L_{ac}^{\ 2}}{2}} \quad \text{(A-13)}$$

$$A_{32} = \frac{-R\left(\frac{L_{dc}L_{ac}}{\sqrt{2}}\sin(2\varphi_0)\right) - 2\omega_0\left(\frac{L_{dc}^{\ 2}L_{ac}}{\sqrt{2}}\cos(2\varphi_0)\right)}{L_{dc}^{\ 3} - \frac{L_{dc}L_{ac}^{\ 2}}{2}} \quad \text{(A-14)}$$

$$A_{33}=\frac{-RL_{dc}^{\ 2}}{L_{dc}^{\ 3}-\frac{L_{dc}L_{ac}^{\ 2}}{2}} \quad \text{(A-15)}$$

$$A_{34}=\frac{-2\left\{\left(\frac{L_{dc}^{\ 2}L_{ac}}{\sqrt{2}}\sin(2\varphi_0)\right)i_{\gamma 0}+\left(\frac{L_{dc}^{\ 2}L_{ac}}{\sqrt{2}}\cos(2\varphi_0)\right)i_{\delta 0}\right\}}{L_{dc}^{\ 3}-\frac{L_{dc}L_{ac}^{\ 2}}{2}} \quad \text{(A-16)}$$

$$A_{35}=\frac{-4\omega_0\left\{-\frac{L_{dc}L_{ac}^{\ 2}}{2}i_{00}\right\}}{L_{dc}^{\ 3}-\frac{L_{dc}L_{ac}^{\ 2}}{2}} \quad \text{(A-17)}$$

$$A_{41}=\frac{\sqrt{2}P^2L_{ac}}{J}i_{00}\sin(2\varphi_0) \quad \text{(A-18)}$$

$$A_{42}=\frac{\sqrt{2}P^2L_{ac}}{J}i_{00}\cos(2\varphi_0) \quad \text{(A-19)}$$

$$A_{43}=\frac{\sqrt{2}P^2L_{ac}}{J}\left(i_{\gamma 0}\sin(2\varphi_0)+i_{\delta 0}\cos(2\varphi_0)\right) \quad \text{(A-20)}$$

$$A_{45}=\frac{\sqrt{2}P^2L_{ac}}{J}\left(2i_{\gamma 0}i_{00}\cos(2\varphi_0)-2i_{\delta 0}i_{00}\sin(2\varphi_0)\right) \quad \text{(A-21)}$$

$$A_{52}=-K_1 \quad \text{(A-22)}$$

$$A_{54}=-1 \quad \text{(A-23)}$$

$$A_{56}=K \quad \text{(A-24)}$$

$$A_{62}=\frac{1}{\tau} \quad \text{(A-25)}$$

$$A_{66}=-\frac{1}{\tau} \quad \text{(A-26)}$$

$$A_{otherwise}=0 \quad \text{(A-27)}$$

$$B_{11}=\frac{L_{dc}^{\ 2}-\frac{L_{ac}^{\ 2}}{2}\sin^2(2\varphi_0)}{L_{dc}^{\ 3}-\frac{L_{dc}L_{ac}^{\ 2}}{2}} \quad \text{(A-28)}$$

$$B_{12}=\frac{-\frac{L_{ac}^{\ 2}}{2}\sin(2\varphi_0)\cos(2\varphi_0)}{L_{dc}^{\ 3}-\frac{L_{dc}L_{ac}^{\ 2}}{2}} \quad \text{(A-29)}$$

$$B_{13}=\frac{-\frac{L_{dc}L_{ac}}{\sqrt{2}}\cos(2\varphi_0)}{L_{dc}^{\ 3}-\frac{L_{dc}L_{ac}^{\ 2}}{2}} \quad \text{(A-30)}$$

$$B_{21}=\frac{-\frac{L_{ac}^{\ 2}}{2}\sin(2\varphi_0)\cos(2\varphi_0)}{L_{dc}^{\ 3}-\frac{L_{dc}L_{ac}^{\ 2}}{2}} \quad \text{(A-31)}$$

$$B_{22}=\frac{L_{dc}^{\ 2}-\frac{L_{ac}^{\ 2}}{2}\cos^2(2\varphi_0)}{L_{dc}^{\ 3}-\frac{L_{dc}L_{ac}^{\ 2}}{2}} \quad \text{(A-32)}$$

$$B_{23}=\frac{\frac{L_{dc}L_{ac}}{\sqrt{2}}\sin(2\varphi_0)}{L_{dc}^{\ 3}-\frac{L_{dc}L_{ac}^{\ 2}}{2}} \quad \text{(A-33)}$$

$$B_{31}=\frac{-\frac{L_{dc}L_{ac}}{\sqrt{2}}\cos(2\varphi_0)}{L_{dc}^{\ 3}-\frac{L_{dc}L_{ac}^{\ 2}}{2}} \quad \text{(A-34)}$$

$$B_{32}=\frac{\frac{L_{dc}L_{ac}}{\sqrt{2}}\sin(2\varphi_0)}{L_{dc}^{\ 3}-\frac{L_{dc}L_{ac}^{\ 2}}{2}} \quad \text{(A-35)}$$

$$B_{33}=\frac{L_{dc}^{\ 2}}{L_{dc}^{\ 3}-\frac{L_{dc}L_{ac}^{\ 2}}{2}} \quad \text{(A-36)}$$

$$B_{14}=2i_{\delta 0} \quad \text{(A-37)}$$

$$B_{24}=-2i_{\gamma 0} \quad \text{(A-38)}$$

$$B_{54}=1 \quad \text{(A-39)}$$

$$B_{otherwise}=0 \quad \text{(A-40)}$$

2. Derivation of (4) and (5)

Relationship between the dq-axis current and the dq-axis current is expressed as in (A41),

$$\begin{bmatrix} i_\gamma \\ i_\delta \\ i_0 \end{bmatrix}=\begin{bmatrix} \cos(2\varphi_0) & \sin(2\varphi_0) & 0 \\ -\sin(2\varphi_0) & \cos(2\varphi_0) & 0 \\ 0 & 0 & 1 \end{bmatrix}\begin{bmatrix} i_d \\ i_q \\ i_0 \end{bmatrix} \quad \text{(A-41)}$$

Equation (5) is derived, substituting (12) and (13) into (A-41) under the assumption that the MTPA control is achieved. The simplified δ-axis voltage is derived by ignoring the asynchronous term appearing as the sixth harmonic for simplification in the steady-state, which is expressed as in (A-42),

$$\begin{aligned} v_\delta &= Ri_\delta+2\omega\left(L_{dc}i_\gamma+\frac{L_{ac}}{\sqrt{2}}\cos(2\varphi_0)i_0\right) \\ &= R\frac{i_0}{\sqrt{2}}\cos(2\varphi_0)+2\omega\frac{i_0}{\sqrt{2}}\left(L_{dc}\sin(2\varphi_0)+L_{ac}\cos(2\varphi_0)\right) \end{aligned} \quad \text{(A-42)}$$

Assuming that the reactive power Q_{dq} in the dq-axis expressed as expressed in (16) is equal to that in the γδ-axis as in (17), (A43) is obtained from (14) and (5).

$$\omega L_{dc}i_0^{\ 2}=v_\delta\frac{i_0}{\sqrt{2}}\sin(2\varphi_0) \quad \text{(A-43)}$$

Substituting (A-42) into (A-43), the deviation angle between the dq-axis and the γδ-axis is expressed as

$$\frac{\omega L_{dc}}{0.5R+\omega L_{ac}}=\frac{\sin(2\varphi_0)}{\cos(2\varphi_0)}=\tan(2\varphi_0) \quad \text{(A-44)}$$

Thus, (4) is derived by solving (A-44) for φ_0.

3. Fine vibration in Fig. 10

App. Fig.1 shows an enlarged waveform of the fine vibrations in the torque waveform immediately after startup in Fig. 10. As shown in App. Fig.1, the frequency of the fine vibrations is 200 Hz.

App. Fig.2 shows the impulse response of the current and torque

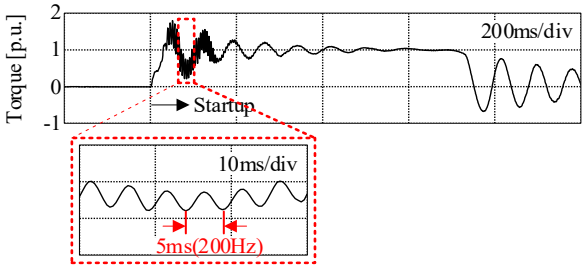

App. Fig.1. Enlarged torque waveform at startup.

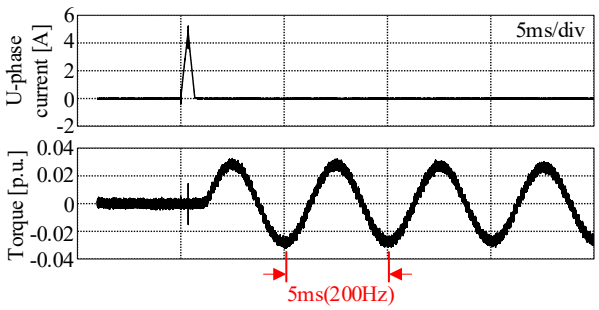

App. Fig.2. Measurement results of resonant frequency.

in the experimental system. The torsional resonance is excited by impulse current, giving a torque shock, as can be seen from the App. Fig.2, the torsional resonance frequency of the experimental system is 200 Hz. This frequency matches the frequency of fine vibrations in the torque waveform immediately after startup. Therefore, the fine vibrations, which differ from ω_n, result from the excitation of the torsional resonance in the experimental system due to the torque step in the startup.

Hirotaka Kato (Student member) received the B.S. degree in electrical, electronics and information engineering from Nagaoka University of Technology, Niigata, Japan, in 2022. He has been with Nagaoka University of Technology as a M.S. course student in electrical, electronics and information engineering. He is a student member of IEEJ.

Takahiro Kumagai (Member) received the B.S. degree in electrical, electronics and information engineering from Nagaoka University of Technology, Niigata, Japan, in 2017. From June to December in 2021, he was with Yokohama National University M&E Energy Conversion Laboratory as a special research student. In 2022, he received the Ph.D. degree in 5-year integrated doctoral program of department of science of technology innovation from Nagaoka University of Technology. He is a member of IEEJ and IEEE. Since 2022, he has been with DENSO Corporation, Aichi, Japan. His current research focuses on the driving method and the motor design method for switched reluctance motor. He received IEEJ Industry Applications Society Distinguished Transaction Paper Award in 2022.

Keisuke Kusaka (Member) received the B.S. and M.S. degrees in electrical, electronics and information from Nagaoka University of Technology, Niigata, Japan in 2011, 2013, respectively. From 2015 to 2016, he was with Swiss Federal Institute of Technology in Lausanne (EPFL), Switzerland as a trainee. In 2016, he received the Ph.D. degree in energy and environment science from Nagaoka University of Technology. He was with Nagaoka University of Technology, Niigata, Japan as a researcher from 2016 to 2018. Since 2018, he has been with Nagaoka University of Technology, Niigata, Japan as an assistant professor. His current research interests include the areas of IPT systems and high-frequency converters. He is a member of Institute of Electrical Engineers of Japan, Society of Automotive Engineers of Japan and the IEEE.

Jun-ichi Itoh (Senior member) received his M.S. and Ph.D. degree in electrical and electronic systems engineering from Nagaoka University of Technology, Niigata, Japan in 1996, 2000, respectively. From 1996 to 2004, he was with Fuji Electric Corporate Research and Development Ltd., Tokyo, Japan. He was with Nagaoka University of Technology, Niigata, Japan as an associate professor. Since 2017, he has been a professor. His research interests are matrix converters, dc/dc converters, power factor correction techniques, energy storage system and adjustable speed drive systems. He received IEEJ Academic Promotion Award (IEEJ Technical Development Award) in 2007. In addition, he also received Isao Takahashi Power Electronics Award in IPEC-Sapporo 2010 from IEEJ, 58th OHM Technology Award from The Foundation for Electrical Science and Engineering, November, 2011, Intelligent Cosmos Award from Intelligent Cosmos Foundation for the Promotion of Science, May, 2012, and Third prize award from Energy Conversion Congress and Exposition-Asia, June, 2013. Prizes for Science and Technology (Development Category) from the Commendation for Science and Technology by the Minister of Education, Culture, Sports, Science and Technology, April 2017. He is a senior member of the Institute of Electrical Engineers of Japan, the Society of Automotive Engineers of Japan and the Institute of Electrical and Electronics Engineers.

Masakazu Kato (Member) received the B.S. and M.S. degrees in electrical, electronics and information from Nagaoka University of Technology, Niigata, Japan in 2012, 2014, respectively. In August 2016, he established Nagaoka Motor Development Co., Ltd. In 2017, he received the Ph.D. degree in energy and environment science from Nagaoka University of Technology. His current research interests include control and simulation of electrical motor.